Fast Adaptive Sparse Iterative Reweighted Super-Resolution Method for Forward-Looking Radar Imaging

Jiawei Luo, *Student Member, IEEE*, Yulin Huang, *Senior Member, IEEE*, Ruitao Li, Deqing Mao, *Member, IEEE*, Yongchao Zhang, *Member, IEEE*, Yin Zhang, *Member, IEEE*, and Jianyu Yang, *Member, IEEE*

***Abstract*—Recently, a sparse super-resolution method based on L_1 iterative reweighted norm (IRN) has been proposed to improve the azimuth resolution of forward-looking radar. However, this method suffers from poor adaptability and high computational complexity due to its noise-sensitive user-parameter and the necessity for high-dimensional matrix inversion. To this end, a fast adaptive L_1-IRN sparse super-resolution method is derived in this article, allowing for the user-parameter-free and efficient sparse imaging of forward-looking radar. First, we establish the super-resolution model of forward-looking radar and analyze the user parameter selection problem in the conventional L_1-IRN method. Second, based on Bayesian theory, adaptive iterative weights of different azimuths are derived by transforming the sparse estimation problem into a maximum posterior (MAP) estimation problem. Finally, by using QR decomposition and Sherman–Morrison formula, the dimensionality of the echo and antenna pattern involved in the iteration is reduced to further diminish the computational complexity. Compared to the existing L_1-IRN method, the proposed method eliminates the need for any user parameters, and the computational complexity has been reduced from $O(JN^3)$ to $O(JN^2a)$. Simulation and measured data demonstrate the superiority of the proposed method.**

***Index Terms*—Forward-looking, radar imaging, super-resolution.**

I. Introduction

RADAR forward-looking imaging technology finds wide applications in aircraft autonomous landing, material airdrop, and terrain mapping [1], [2], [3], [4], [5]. However, traditional Doppler beam sharpening and synthetic aperture radar techniques encounter difficulties in enhancing the imaging resolution of the forward-looking area due to the reduction in Doppler gradient [6], [7], [8].

Real aperture radar (RAR) is frequently employed for forward-looking imaging due to its omnidirectional capability. Nevertheless, its resolution is determined by the size of the antenna aperture. While a larger antenna can enhance resolution, it requires more spatial resources. This tension between needing larger antennas and the constraints of small platforms restricts RAR's azimuth resolution, thereby limiting its use in airborne forward-looking imaging [9], [10].

To alleviate the above issue, scholars have proposed various azimuth super-resolution imaging methods, including spectral estimation methods [11], [12], [13], Bayesian methods [14], [15], [16], and regularization methods [17], [18], [19], [20]. In [11], a fast conjugate gradient iterative adaptive super-resolution algorithm is proposed for forward-looking radar imaging. This method accurately represents the azimuth and elevation velocity migration for airborne platform, eliminates the range and azimuth-elevation coupling, improving the azimuth and elevation resolution. Based on Bayesian theory, Chen et al. [14] proposed an efficient Bayesian forward super-resolution imaging algorithm grounded on Doppler deconvolution in extended beam space, which transforms the imaging problem into a convex optimization problem and improved the performance of forward imaging. Utilizing the regularization framework [17], a truncated singular value decomposition forward-looking super-resolution imaging algorithm is proposed, combined with the total variation norm. This algorithm preserves contours even under low signal-to-noise ratio (SNR) conditions and achieves high-quality imaging results.

Recently, the sparse reconstruction problem has garnered significant attention and discussion [21], [22], [23]. For sparse target scenes such as ships in ports and aircraft in airports, Tuo et al. [21] proposed a sparse super-resolution method based on the L_1 norm. This method effectively addresses the issue by minimizing the L_1 norm to enhance the imaging resolution of scanning radar. However, this method faces several challenges. First, its penalty parameter requires manual adjustment according to the actual environment and exhibits poor adaptive capability due to sensitivity to noise. The L-curve can serve as a guideline for selection, but it necessitates prior knowledge of the SNR and may not always be reliable [5]. To solve this problem, a

Received 30 April 2024; revised 14 September 2024; accepted 8 October 2024. Date of publication 23 October 2024; date of current version 6 November 2024. This work was supported in part by the China Postdoctoral Science Foundation under Grant BX20220055, and Grant 2022M720667, and in part by the Municipal Government of Quzhou Grant 2023D026. *(Corresponding author: Yulin Huang.)*

Jiawei Luo, Ruitao Li, Deqing Mao, and Jianyu Yang are with the School of Information and Communication Engineering, University of Electronic Science and Technology of China, Chengdu 611731, China.

Yulin Huang, Yongchao Zhang, and Yin Zhang are with the School of Information and Communication Engineering, University of Electronic Science and Technology of China, Chengdu 611731, China, and also with the Yangtze Delta Region Institute, University of Electronic Science and Technology of China, Quzhou 324000, China (e-mail: yulinhuang@uestc.edu.cn).

Digital Object Identifier 10.1109/JSTARS.2024.3485091

weak-depended method was proposed in [24], which reduces the influence of parameters on super-resolution imaging. However, this method can only attenuate the parameter influence, not self-adjust. Second, each iteration of the method necessitates the computation of the inverse of a high-dimensional matrix, resulting in exceedingly high computational complexity. These factors render the method unsuitable for hardware implementation and practical engineering applications.

To address these challenges, this article presents a novel approach: A fast adaptive L_1 iterative reweighted norm (L_1-IRN) method with no user parameters and low complexity. First, the echo model of scanning radar is established and the issue of user parameter selection in traditional L_1-IRN methods is analyzed. Second, leveraging Bayesian criterion, the maximum posterior (MAP) estimation of the target scattering coefficient $\mathbf{m}$ and echo $\mathbf{y}$ is derived. Subsequently, an adaptive iterative weighted parameter is obtained by substituting probabilistic models $P(\mathbf{m})$ and $P(\mathbf{y}|\mathbf{m})$ into the objective function. Third, an orthogonal matrix is constructed through QR decomposition to reduce the dimensionality of antenna pattern function $\mathbf{D}$ and the echo $\mathbf{y}$. Finally, employing the Sherman–Morrison formula, the operation of high-dimensional matrices is transformed into low-dimensional matrix operations to achieve the low-complexity forward-looking super-resolution target scattering reconstruction. Compared to existing L_1-IRN methods, the proposed method boasts several advantages. First, it completely eliminates the need for user parameters and exhibits excellent adaptive capabilities. In addition, there is no requirement to compute the inverse of high-dimensional matrices, significantly reducing computational complexity compared to traditional L_1 methods. This feature facilitates the hardware implementation of the algorithm.

The rest of this article is organized as follows. Section II introduces the echo model of the forward-looking scanning radar. Section III presents a comprehensive overview of the proposed method. Sections IV and V provide the simulation and measured data results. Finally, Section VI concludes this article.

II. Echo Model

The geometric motion model of the forward-looking scanning radar is depicted in Fig. 1. The height of the aircraft is H. The velocity along the Y-axis is v, and the radar beam scans counterclockwise with an angular velocity ω. The pitch angle of the beam is α, and at time $t = 0$, the aircraft is located at point A. Assuming there is a target P in the space at time t, with P located at a distance R_0 from point A, and having a horizontal azimuth of φ_0 and a spatial azimuth of θ_0. Geometric relations yield $\cos\theta_0 = \cos\varphi_0 \cos\alpha$.

Suppose that at time t, the aircraft moves from point A to point B and the horizontal azimuth of the target P relative to the aircraft is φ and the spatial azimuth is θ, then the distance between the aircraft and the target P can be expressed as follows:

$$R(t) = \sqrt{R_0^2 + (vt)^2 - 2R_0 vt\cos\theta_0}. \tag{1}$$

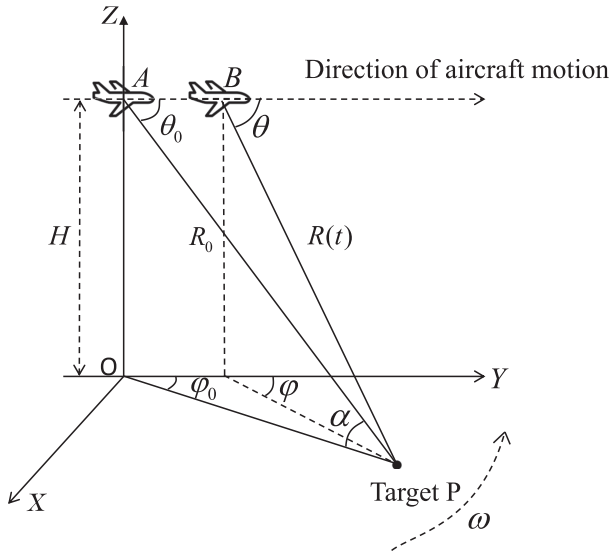

Fig. 1. Geometric motion model of forward-looking scanning radar.

The Taylor series expansion of $R(t)$ at $t = 0$ yields as follows:

$$R(t) = R_0 - v\cos\theta_0 t + \frac{v^2\sin^2\theta_0}{2R_0}t^2. \tag{2}$$

Based on literature [17] and [25], ignoring the influence of the quadratic term in the above formula, $R(t)$ can be approximated as follows:

$$R(t) \approx R_0 - v\cos\theta_0 t. \tag{3}$$

Forward-looking scanning radar emits large bandwidth linear frequency modulation (FM) signals, such that

$$S(\tau) = \text{rect}\left(\frac{\tau}{T_r}\right)\exp\left(j2\pi f_0\tau + j\pi K_r\tau^2\right) \tag{4}$$

where τ is the fast time variable in range direction, T_r is the pulsewidth of the linear FM signal, f_0 is the carrier frequency, K_r is the FM slope, and rect$(\cdot)$ is the rectangular window function of width T_r.

For the target P, the echo signal after down-conversion can be expressed as follows:

$$S(\tau,t) = \sigma_0 f(t)\text{rect}\left(\frac{\tau-\tau_d}{T_r}\right)\exp\left(j\pi K_r(\tau-\tau_d)^2\right)$$
$$\exp\left(-j2\pi f_0\tau_d\right) \tag{5}$$

where σ_0 is the target scattering coefficient of P, $f(t)$ is the antenna pattern modulation function, t is the slow time variable in azimuth direction, $\tau_d = 2R(t)/c$ is the echo delay, and c is the speed of the electromagnetic wave.

By pulse compression of the echo signal, we can obtain the following:

$$S_{\text{rc}}(\tau,t) = \sigma_0 f(t)\text{sinc}\left[B(\tau-\tau_d)\right]\exp\left(-j2\pi f_0\tau_d\right) \tag{6}$$

where sinc$[\cdot]$ is the range pulse compression response function and B is the transmitted signal bandwidth.

After pulse compression, for low-speed platforms, the Doppler term $\exp(-j2\pi f_0\tau_d)$ is ignored. Considering all targets within the detection range, it can be observed that the azimuth echo can be represented as a convolution of the azimuth antenna pattern function and target scattering, illustrated as follows:

$$\bar{S}_{\text{rc}}(\tau,t)=\iint \sigma_0 f(t)\text{sinc}\left[B(\tau-\tau_d)\right]\text{d}\tau\text{d}t. \tag{7}$$

Assuming the range and azimuth angle of a random target in this space is R and θ, we can get the following:

$$\begin{cases}\tau=\frac{2R}{c}\\ t=\frac{\theta-\theta_0}{\omega}.\end{cases} \tag{8}$$

Substituting (8) into (7) can obtain the following:

$$\bar{S}_{\text{rc}}(R,\theta)=\iint \sigma_0 f(\theta-\theta_0)\,\text{sinc}\left[\frac{2B}{c}(R-R_d)\right]\text{d}R\text{d}\theta. \tag{9}$$

Equation (9) can be written in convolution form as follows:

$$\bar{S}_{\text{rc}}(R,\theta)=h(R,\theta)*\sigma(R,\theta) \tag{10}$$

where $h(R,\theta)$ is the antenna pattern function and $\sigma(R,\theta)$ represents the effective scattering function. Consider additive noise $n(R,\theta)$, we have

$$\bar{S}_{\text{rc}}(R,\theta)=h(R,\theta)*\sigma(R,\theta)+n(R,\theta). \tag{11}$$

For a certain range bin, discretization of (11) yields [26], [27] as follows:

$$\mathbf{y}=\mathbf{D}\mathbf{m}+\mathbf{n} \tag{12}$$

where $\mathbf{y}\in\mathbb{C}^N$ represents the echo, N is the sampling number of azimuthal echo, $\mathbf{m}\in\mathbb{C}^N$ is the scattering coefficient of the target, $\mathbf{n}\in\mathbb{C}^N$ is the additive noise, and $\mathbf{D}\in\mathbb{C}^{N\times N}$ is the antenna pattern matrix, respectively. In this article, the echo is disregarded during the scanning of the beam in and out of the scene, leading to the consideration of a truncated antenna pattern matrix [28], which can be precisely formulated as follows:

$$\mathbf{D}=\begin{bmatrix} d_{(\theta_0)} & \cdots & d_{(\theta_{-l})} & & \\ \vdots & \ddots & & \ddots & \\ d_{(\theta_l)} & & \ddots & & d_{(\theta_{-l})} \\ & \ddots & & \ddots & \vdots \\ & & d_{(\theta_l)} & \cdots & d_{(\theta_0)} \end{bmatrix}_{N\times N} \tag{13}$$

where $[d_{(\theta_{-l})}\ldots d_{(\theta_0)}\ldots d_{(\theta_l)}]$ represents samples of the antenna pattern, with the count of samples being governed by the pulse repetition frequency, beamwidth, and antenna scanning velocity.

III. Proposed Method

In this section, the conventional L_1-IRN method was reviewed, and its parameter selection issues were analyzed. Then, an adaptive method utilizing iterative weight parameters is derived based on Bayesian theory. Finally, the computational complexity of the algorithm is reduced by employing the matrix dimension reduction strategy.

A. Conventional L_1-IRN Method

Recovering the scattering coefficient $\mathbf{m}$ from the echo $\mathbf{y}$ poses a challenging ill-posed issue. To relax this ill-posedness, regularization methods can be employed, incorporating constraints on unknown variables during the inverse solution process.

The conventional regularization function can be represented as follows:

$$\hat{\mathbf{m}}=\text{argmin}\frac{1}{p}\|\mathbf{y}-\mathbf{D}\mathbf{m}\|_p^p+\lambda\frac{1}{q}\|\mathbf{m}\|_q^q \tag{14}$$

where the selected norm type determines the values of p and q. $\frac{1}{p}\|\mathbf{y}-\mathbf{D}\mathbf{m}\|_p^p$ represents the term related to data fitting, while $\frac{1}{q}\|\mathbf{m}\|_q^q$ signifies penalty term. The regularization parameter λ ensures a balance between the sparsity of s and the amplification of noise.

In terms of sparse super-resolution issues, the L_q norm, where $0\leqslant q\leqslant 1$, is typically utilized as the penalty function. A smaller q indicates a stronger sparse requirement. Therefore, the value of q should be minimized in theory. When $0\leqslant q\leqslant 1$, obtaining the global optimum solution is challenging. Hence, the sparse characteristics of the L_1 norm are commonly employed to characterize the target.

When the values of p and q are 2 and 1, respectively, the super-resolution problem of scanning radar can typically be expressed as an optimization problem constrained by the L_1 norm. Referencing [21], the objective function is established with regularization imposed via the L_1 norm and fidelity constrained to minimize error energy. Thus, the optimization problem can be articulated as follows:

$$\hat{\mathbf{m}}=\underset{\mathbf{m}}{\text{argmin}}||\mathbf{y}-\mathbf{D}\mathbf{m}||_2^2+\lambda||\mathbf{m}||_1 \tag{15}$$

where λ is the regularization parameter.

Employing IRN to tackle the above problem, the iterative procedure can be outlined as follows [21]:

$$\mathbf{m}_{j+1}=\left(\mathbf{D}^T\mathbf{D}+\lambda\mathbf{Q}_j\right)^{-1}\mathbf{D}^T\mathbf{y} \tag{16}$$

where j represents the number of iterations, $\mathbf{Q}_j=\text{diag}\left(|\mathbf{m}_j|^{-1}\right)$.

While this approach enhances angular resolution, it is important to note the presence of a user-defined parameter λ in the iterative process of IRN. This parameter necessitates manual adjustment. However, λ proves to be highly sensitive to noise, undermining the robustness and adaptability of IRN.

A curve of the mean square error (MSE) changing with λ, when λ varies from 0.001 to 20, is given in Fig. 2. It can be seen that with the increase of λ, the value of MSE first decreases and then increases. In our simulations, a smaller λ yields higher resolution but compromises noise immunity. Conversely, a larger λ results in lower resolution but smoother outcomes. The above two cases will lead to the increase of MSE value. Therefore, to obtain the expected imaging results, it is necessary to set the value of λ with the smallest MSE in Fig. 2 when adjusting the parameter λ, which can maintain a good balance between lower noise and better resolution. However, for the measured data without reference values, it is almost impossible to find the optimal λ manually.

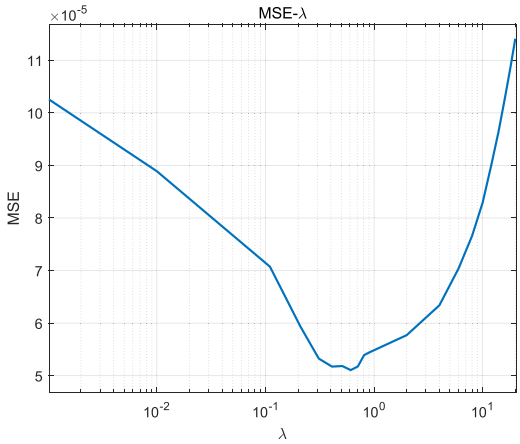

Fig. 2. MSE versus λ.

B. Adaptive L_1-IRN Method

In this section, the adaptive L_1-IRN sparse super-resolution algorithm designed for scanning radar was developed, leveraging on the principles outlined in [7]. We have crafted a more robust method for computing $\lambda \mathbf{Q}_j$ in (16) by transforming the sparsity estimation challenge (15) into a maximum a posteriori (MAP) estimation problem.

In (15), the parameter λ serves as a constant factor balancing the L_1 norm sparse regularization term and the data fidelity term. Research has demonstrated that employing reweighted L_1 norm sparsity yields results closer to the L_1 norm sparsity compared to using constant weights. This adjustment enhances the reconstruction of sparse signals, prompting the rewriting of the L_1 norm in (15) as follows:

$$\lambda \|\mathbf{m}\|_1 = \sum_{i=1}^{K} \lambda_i |m_i|. \tag{17}$$

Based on Bayesian theory, the MAP estimate of $\mathbf{m}$ and $\mathbf{y}$ can be written as follows:

$$\hat{\mathbf{m}} = \underset{\mathbf{m}}{\operatorname{argmax}} \left\{ \log P\left(\mathbf{m}|\mathbf{y}\right) \right\}. \tag{18}$$

Equation (18) can be simplified as follows:

$$\hat{\mathbf{m}} = \underset{\mathbf{m}}{\operatorname{argmin}} \left\{ -\log P\left(\mathbf{y}|\mathbf{m}\right) - \log P\left(\mathbf{m}\right) \right\} \tag{19}$$

where $P(\mathbf{y}|\mathbf{m})$ represents the likelihood function and $P(\mathbf{m})$ represents the prior information of the target. Assuming that noise $\mathbf{e}$ follows a Gaussian distribution with zero mean and σ_n variance, the likelihood function can be written as follows:

$$P(\mathbf{y}|\mathbf{m}) = \frac{1}{\sigma_n \sqrt{2\pi}} \exp\left(-\frac{1}{2{\sigma_n}^2} \|\mathbf{y} - \mathbf{D}\mathbf{m}\|_2^2 \right). \tag{20}$$

The prior distribution of $P(\mathbf{m})$ usually satisfies a Laplacian probability model with zero means as follows:

$$P(\mathbf{m}) = \prod_{i=1}^{K} \frac{1}{\sqrt{2}\gamma_i} \exp\left(-\frac{\sqrt{2}}{\gamma_i} |m_i| \right) \tag{21}$$

where γ_i is the variance of m_i. By replacing the L_1 norm in (15) with (17), the resultant expression is as follows:

$$\hat{\mathbf{m}} = \underset{\mathbf{m}}{\operatorname{argmax}} \|\mathbf{y} - \mathbf{D}\mathbf{m}\|_2^2 + \sum_{i=1}^{K} \lambda_i |m_i|. \tag{22}$$

According to the principle of logarithmic operation, (19) can be rewritten as follows:

$$\hat{\mathbf{m}} = \operatorname{argmin} - \left\{ \log \left[P\left(\mathbf{y}|\mathbf{m}\right) P\left(\mathbf{m}\right) \right] \right\}. \tag{23}$$

By bringing $P(\mathbf{y}|\mathbf{m})$ from (20) and $P(\mathbf{m})$ from (21) into (23), the resultant expression is as follows:

$$\hat{\mathbf{m}} = \underset{\mathbf{m}}{\arg\min} - \left\{ \log \prod_{i=1}^{K} \frac{1}{2\sqrt{\pi}\gamma_i \sigma_n} + \log \exp \left(-\frac{1}{2{\sigma_n}^2} \|\mathbf{y} - \mathbf{D}\mathbf{m}\|_2^2 - \sum_{i=1}^{K} \frac{\sqrt{2}}{\gamma_i} |m_i| \right) \right\}. \tag{24}$$

Further simplifying (24) yields the following:

$$\hat{\mathbf{m}} = \underset{\mathbf{m}}{\arg\min} - \log \prod_{i=1}^{K} \frac{1}{2\sqrt{\pi}\gamma_i \sigma_n} + \frac{1}{2{\sigma_n}^2} \|\mathbf{y} - \mathbf{D}\mathbf{m}\|_2^2 + \sum_{i=1}^{K} \frac{\sqrt{2}}{\gamma_i} |m_i|. \tag{25}$$

It is apparent that $2\sigma_n^2$ is a constant that has no effect on the estimation of $\mathbf{m}$. The first component of (25) is not related to $\mathbf{m}$ and does not influence its estimation.

$$\hat{\mathbf{m}} = \underset{\mathbf{m}}{\arg\min} \|\mathbf{y} - \mathbf{D}\mathbf{m}\|_2^2 + \sum_{i=1}^{K} \frac{2\sqrt{2}{\sigma_n}^2}{\gamma_i} |m_i|. \tag{26}$$

By matching the coefficients of corresponding terms in (22) and (26), the iterative equation for the weighting parameter λ_i can be derived as follows:

$$\lambda_i = \frac{2\sqrt{2}\hat{\sigma}_n^2}{\gamma_i}. \tag{27}$$

To ensure numerical stability, we can rewrite the iterative equation for the weighted parameters λ_i as follows:

$$\lambda_i = \frac{2\sqrt{2}\hat{\sigma}_n^2}{\hat{\gamma}_i + \varepsilon} \tag{28}$$

where $\hat{\gamma}_i$ represents the estimate of γ_i, $\hat{\sigma}_n^2$ represents the estimate of noise power ${\sigma_n}^2$, and ε is a constant used to keep the value stable, respectively. The estimation of noise power $\hat{\sigma}_n^2$ can be expressed as follows:

$$\hat{\sigma}_n^2 = \frac{1}{N} \|\mathbf{y} - \mathbf{D}\mathbf{m}_j\|_2^2 \tag{29}$$

where $\mathbf{m}_j$ represents the target scattering estimate for the jth iteration. The iterative updating expression of adaptive parameter based on IRN can be written as follows:

$$\mathbf{m}_{j+1} = \left(\mathbf{D}^T\mathbf{D} + \operatorname{diag}\left(\boldsymbol{\lambda} \cdot (\mathbf{m}_j)^{-1} \right) \right)^{-1} \mathbf{D}^T\mathbf{y} \tag{30}$$

where $\boldsymbol{\lambda} = [\lambda_1, \lambda_2, \ldots, \lambda_k]$ is calculated from (28) and $\mathbf{m}_0 = (\mathbf{D}^T\mathbf{D} + \mathbf{I})^{-1}\mathbf{D}^T\mathbf{y}$.

C. Fast Adaptive L_1-IRN Method

In the previous section, the iterative (30) for the adaptive L_1-IRN method was obtained. While this approach offers the flexibility to dynamically update the regularization parameter λ, the matrix inverse operation $(\mathbf{D}^T\mathbf{D} + \mathrm{diag}(\boldsymbol{\lambda} \cdot (\mathbf{m}_j)^{-1}))^{-1}$ required in every iteration poses a significant challenge, resulting in exceptionally high computational complexity.

A fast implementation approach for the adaptive L_1-IRN method is proposed to mitigate this challenge. It accomplishes dimensionality reduction of high-dimensional matrices through QR decomposition, effectively reducing computational complexity while preserving essential information. QR decomposition can decompose a matrix into the product of an orthogonal matrix and an upper triangular matrix. Assuming $\mathbf{B}$ is an $m \times n$ matrix, then QR decomposition is to find an orthogonal matrix $\hat{\mathbf{Q}}$ of $m \times m$ and an upper triangular matrix $\hat{\mathbf{R}}$ of $m \times n$.

To construct matrix $\hat{\mathbf{Q}}$, the initial step involves forming a random matrix $\mathbf{T}_{(N\times a)}$, where N is the length of the column echo signal and a is the target dimension of dimensionality reduction. Based on the theory in [27], a can be adaptively determined by the antenna size, wavelength, and scanning range. Define matrix $\mathbf{Y}$ as follows:

$$\mathbf{Y} = \mathbf{D}\mathbf{T}_{(N\times a)}. \tag{31}$$

Then, QR decomposition is performed on the transformed matrix $\mathbf{Y}$ to obtain the orthogonal matrix $\hat{\mathbf{Q}}_{N\times N}$. Since we want to reduce dimension to dimension a, we select the first a columns from matrix $\hat{\mathbf{Q}}_{N\times N}$ to get the matrix $\mathbf{Q}$.

Using the constructed matrix $\mathbf{Q}$ to reduce the dimension of the antenna pattern function $\mathbf{D}$ and echo $\mathbf{y}$, it can be obtained as follows:

$$\begin{cases} \bar{\mathbf{y}} = \mathbf{Q}^T\mathbf{y} \\ \bar{\mathbf{D}} = \mathbf{Q}^T\mathbf{D}. \end{cases} \tag{32}$$

After dimension reduction, the computational complexity of (30) decreases from $4N^3 + N$ to $N^3 + 3N^2a + N$. However, the dimension of the inverse matrix $(\bar{\mathbf{D}}^T\bar{\mathbf{D}} + \mathrm{diag}(\boldsymbol{\lambda} \cdot (\mathbf{m}_j)^{-1}))^{-1}$ remains $N^3 + N^2a + N$. To further reduce the complexity, we utilize the Sherman–Morrison formula [29] to change the order of $\bar{\mathbf{D}}^T$ and $\bar{\mathbf{D}}$ in the inverse matrix.

Based on the Sherman–Morrison equation, we can derive the iterative updating expression of fast adaptive L_1-IRN method from the iterative updating expression of adaptive L_1-IRN method. Suppose $\mathbf{U} = \bar{\mathbf{D}}^T\bar{\mathbf{D}} + \mathrm{diag}(\boldsymbol{\lambda} \cdot (\mathbf{m}_j)^{-1})$. Then, we have as follows:

$$\begin{aligned} &\mathbf{U}\left(\mathrm{diag}\left(\boldsymbol{\lambda} \cdot (\mathbf{m}_j)^{-1}\right)\right)^{-1} \\ &= \mathbf{D}^T\mathbf{D}\left(\mathrm{diag}\left(\boldsymbol{\lambda} \cdot (\mathbf{m}_j)^{-1}\right)\right)^{-1} + \mathbf{I}. \end{aligned} \tag{33}$$

A new weighting matrix is defined as $\mathbf{W}_j$ as follows:

$$\mathbf{W}_j = \left(\mathrm{diag}\left(\boldsymbol{\lambda} \cdot (\mathbf{m}_j)^{-1}\right)\right)^{-1}. \tag{34}$$

Substituting (34) into (33)

$$\mathbf{U}\mathbf{W}_j = \bar{\mathbf{D}}^T\bar{\mathbf{D}}\mathbf{W}_j + \mathbf{I}. \tag{35}$$

Multiply both sides on the right by $\bar{\mathbf{D}}^T$ as follows:

$$\mathbf{U}\mathbf{W}_j\bar{\mathbf{D}}^T = \bar{\mathbf{D}}^T\bar{\mathbf{D}}\mathbf{W}_j\bar{\mathbf{D}}^T + \bar{\mathbf{D}}^T. \tag{36}$$

It can be obtained after reorganizing (36) as follows:

$$\mathbf{U}\mathbf{W}_j\bar{\mathbf{D}}^T = \bar{\mathbf{D}}^T\left(\mathbf{I} + \bar{\mathbf{D}}\mathbf{W}_j\bar{\mathbf{D}}^T\right). \tag{37}$$

Since $(\bar{\mathbf{D}}\mathbf{W}_j\bar{\mathbf{D}}^T + \mathbf{I})$ is invertible, by multiplying both sides on the right by it, we can get the following:

$$\mathbf{U}\mathbf{W}_j\bar{\mathbf{D}}^T\left(\mathbf{I} + \bar{\mathbf{D}}\mathbf{W}_j\bar{\mathbf{D}}^T\right)^{-1} = \bar{\mathbf{D}}^T. \tag{38}$$

Multiplying each side by $\bar{\mathbf{D}}$ followed by adding ${\mathbf{W}_j}^{-1}$ yields the following result:

$$\begin{aligned} &\mathbf{U}\mathbf{W}_j\bar{\mathbf{D}}^T\left(\mathbf{I} + \bar{\mathbf{D}}\mathbf{W}_j\bar{\mathbf{D}}^T\right)^{-1}\bar{\mathbf{D}} + {\mathbf{W}_j}^{-1} \\ &= \bar{\mathbf{D}}^T\bar{\mathbf{D}} + {\mathbf{W}_j}^{-1} \\ &= \mathbf{U}. \end{aligned} \tag{39}$$

After tidying up, we have

$${\mathbf{W}_j}^{-1} = \mathbf{U}\left(\mathbf{I} - \mathbf{W}_j\bar{\mathbf{D}}^T\left(\bar{\mathbf{D}}\mathbf{W}_j\bar{\mathbf{D}}^T + \mathbf{I}\right)^{-1}\bar{\mathbf{D}}\right). \tag{40}$$

Move $\mathbf{U}$ to the left side of the equation as follows:

$$\mathbf{U}^{-1}{\mathbf{W}_j}^{-1} = \mathbf{I} - \mathbf{W}_j\bar{\mathbf{D}}^T\left(\mathbf{I} + \bar{\mathbf{D}}\mathbf{W}_j\bar{\mathbf{D}}^T\right)^{-1}\bar{\mathbf{D}}. \tag{41}$$

Then, we have the lower complexity expression for $\mathbf{U}$ as follows:

$$\begin{aligned} &\left(\bar{\mathbf{D}}^T\bar{\mathbf{D}} + \mathrm{diag}\left(\boldsymbol{\lambda} \cdot (\mathbf{m}_j)^{-1}\right)\right)^{-1} \\ &= \mathbf{W}_j - \mathbf{W}_j\bar{\mathbf{D}}^T\left(\mathbf{I} + \bar{\mathbf{D}}\mathbf{W}_j\bar{\mathbf{D}}^T\right)^{-1}\bar{\mathbf{D}}\mathbf{W}_j \end{aligned} \tag{42}$$

where the dimension of the matrix to be inverted is reduced from N to a. The recurrent representation for the fast adaptive L_1-IRN method is formulated as follows:

$$\bar{\mathbf{m}}_{j+1} = \left(\mathbf{W}_j - \mathbf{W}_j\bar{\mathbf{D}}^T\left(\mathbf{I} + \bar{\mathbf{D}}\mathbf{W}_j\bar{\mathbf{D}}^T\right)^{-1}\bar{\mathbf{D}}\mathbf{W}_j\right)\bar{\mathbf{D}}^T\bar{\mathbf{y}} \tag{43}$$

where $\bar{\mathbf{m}}_0 = (\mathbf{I}_{N\times N} - \bar{\mathbf{D}}^T(\mathbf{I}_{a\times a} + \bar{\mathbf{D}}\bar{\mathbf{D}}^T)^{-1}\bar{\mathbf{D}})\bar{\mathbf{D}}^T\bar{\mathbf{y}}$, $\mathbf{I}$ is the identity matrix. The pseudocode of the algorithm is as follows:

$$Initialize: \bar{\mathbf{m}}_0 = \left(\mathbf{I}_{N\times N} - \bar{\mathbf{D}}^T\left(\mathbf{I}_{a\times a} + \bar{\mathbf{D}}\bar{\mathbf{D}}^T\right)^{-1}\bar{\mathbf{D}}\right)\bar{\mathbf{D}}^T\bar{\mathbf{y}}$$

$$for\ j = 0, 1, 2, \cdots$$

$$\boldsymbol{\lambda} = \frac{2\sqrt{2}\frac{1}{N}\left\|\mathbf{y} - \mathbf{D}\mathbf{m}_j\right\|_2^2}{\hat{\gamma}_i + \varepsilon}$$

$$\mathbf{W}_j = \left(diag\left(\boldsymbol{\lambda} \cdot (\mathbf{m}_j)^{-1}\right)\right)^{-1}$$

$$\bar{\mathbf{m}}_{j+1} = \left(\mathbf{W}_j - \mathbf{W}_j\bar{\mathbf{D}}^T\left(\mathbf{I} + \bar{\mathbf{D}}\mathbf{W}_j\bar{\mathbf{D}}^T\right)^{-1}\bar{\mathbf{D}}\mathbf{W}_j\right)\bar{\mathbf{D}}^T\bar{\mathbf{y}}$$

$$end$$

TABLE I
COMPUTATIONAL COMPLEXITY ANALYSIS

Method	Multiply and divide operation	Computational complexity
Traditional L_1-IRN Method	$J\left(4N^3+N\right)$	$O\left(JN^3\right)$
Adaptive L_1-IRN method	$J\left(4N^3+N\right)$	$O\left(JN^3\right)$
Fast adaptive L_1-IRN method	$J\left(4N^2a+2Na^2+a^3+5N\right)$	$O\left(JN^2a\right)$

D. Complexity Analysis

Since $\mathbf{Q}_j$ is the identity matrix of $N \times N$, the computational complexity of $\lambda\mathbf{Q}_j$ is N. The computational complexity of $\mathbf{D}^T\mathbf{D}+\lambda\mathbf{Q}_j$ is N^3+N, and its computational complexity after inversion is $2N^3+N$. In summary, the computational complexity of the initialization equation $\mathbf{m}_{j+1} = (\mathbf{D}^T\mathbf{D}+\lambda\mathbf{Q}_j)^{-1}\mathbf{D}^T\mathbf{y}$ is $4N^3+N$.

The computational complexity of operation $\mathbf{I}_{a\times a}+\bar{\mathbf{D}}\bar{\mathbf{D}}^T$ is Na^2. Since it is an $a \times a$ matrix after operation, its computational complexity after inversion is Na^2+a^3. Therefore, the computational complexity of operation $\mathbf{I}_{N\times N}-\bar{\mathbf{D}}^T(\mathbf{I}_{a\times a}+\bar{\mathbf{D}}\bar{\mathbf{D}}^T)^{-1}\bar{\mathbf{D}}$ is $2N^2a+2Na^2+a^3$. In summary, the computational complexity of the initialization equation $\bar{\mathbf{m}}_0 = (\mathbf{I}_{N\times N}-\bar{\mathbf{D}}^T(\mathbf{I}_{a\times a}+\bar{\mathbf{D}}\bar{\mathbf{D}}^T)^{-1}\bar{\mathbf{D}})\bar{\mathbf{D}}^T\bar{\mathbf{y}}$ is $4N^2a+2Na^2+a^3$.

The computational complexity of iterative equation $\bar{\mathbf{m}}_{j+1} = (\mathbf{W}_j-\mathbf{W}_j\bar{\mathbf{D}}^T(\mathbf{I}+\bar{\mathbf{D}}\mathbf{W}_j\bar{\mathbf{D}}^T)^{-1}\bar{\mathbf{D}}\mathbf{W}_j)\bar{\mathbf{D}}^T\bar{\mathbf{y}}$ is $4N^2a+2Na^2+a^3+5N$, the calculation of which is the same as the computation that we have made before. In conclusion, the complexity of the proposed fast adaptive L_1-IRN method is $O(JN^2a)$.

According to the above derivation, the algorithm complexity comparison of traditional L_1-IRN method, adaptive L_1-IRN method and fast adaptive L_1-IRN method is shown in Table I. It can be seen that the computational complexity has been reduced from $O(JN^3)$ to $O(JN^2a)$.

IV. SIMULATION

In this section, point target simulation and surface target simulation are conducted using the traditional L_1-IRN method with different regularized parameter, the adaptive L_1-IRN method, and the fast adaptive L_1-IRN method. The simulation results of these three methods will be compared to demonstrate the effectiveness of the proposed fast adaptive L_1-IRN method. The simulation is performed on a 12th Gen Intel Core i9-12900H processor with 64GB RAM, using Windows 11 and MATLAB 2021.

A. Point Target Simulation

To validate the effectiveness of the proposed method, this section conducts point target simulation. The simulation environment parameters are listed in Table II.

1) Profile Results: The original scene of point targets is depicted in Fig. 3, where targets with identical amplitudes are positioned at -1° and 1°. Fig. 4(a) illustrates the echo with a SNR of 20 dB. Because the beam width is larger than the target interval, the echo energy of the two targets is aliased. We conducted 10 Monte Carlo tests for each super-resolution method, with results shown in Fig. 4(b)–(f). When $\lambda = 0.1$, the imaging result of the traditional L_1-IRN method is shown in Fig. 4(b). It can be seen that it has high resolution, but it will amplify the noise, resulting in many identification errors in the imaging result. When $\lambda = 10$, the imaging result of traditional L_1-IRN method is shown in Fig. 4(c). When $\lambda = 50$, the result of the previous method is shown in Fig. 4(d). It can be observed that its noise is reduced compared to the previous two parameters, but the resolution is also decreased. Fig. 4(e) exhibits the imaging result of the adaptive L1-IRN method, demonstrating superior resolution and noise suppression compared to the traditional L_1-IRN method. Finally, Fig. 4(f) presents the imaging result of the fast adaptive L_1-IRN method, indicating that the acceleration step does not compromise resolution.

TABLE II
SIMULATION PARAMETERS OF THE POINT TARGET

Parameter	Value
Azimuth scanning range	-10°–10°
Azimuth beamwidth	3°
Scanning speed	$60^\circ/\mathrm{s}$
Pulse repetition frequency	1000 Hz

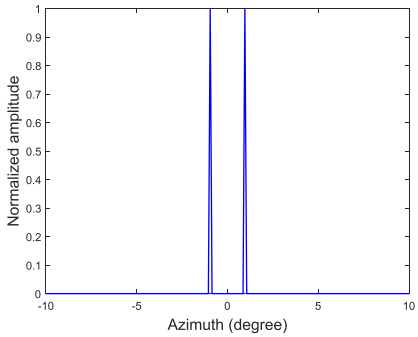

Fig. 3. Original scene of point target.

2) Quantitative Analysis: MSE is introduced in this article to measure the performance of the reconstruction quality. The smaller the value of MSE, the better the performance of the super-resolution method. MSE can be defined as follows:

$$\mathrm{MSE} = \frac{1}{S}\sum_{i=1}^{S}(\hat{m}_i - m_i)^2 \tag{44}$$

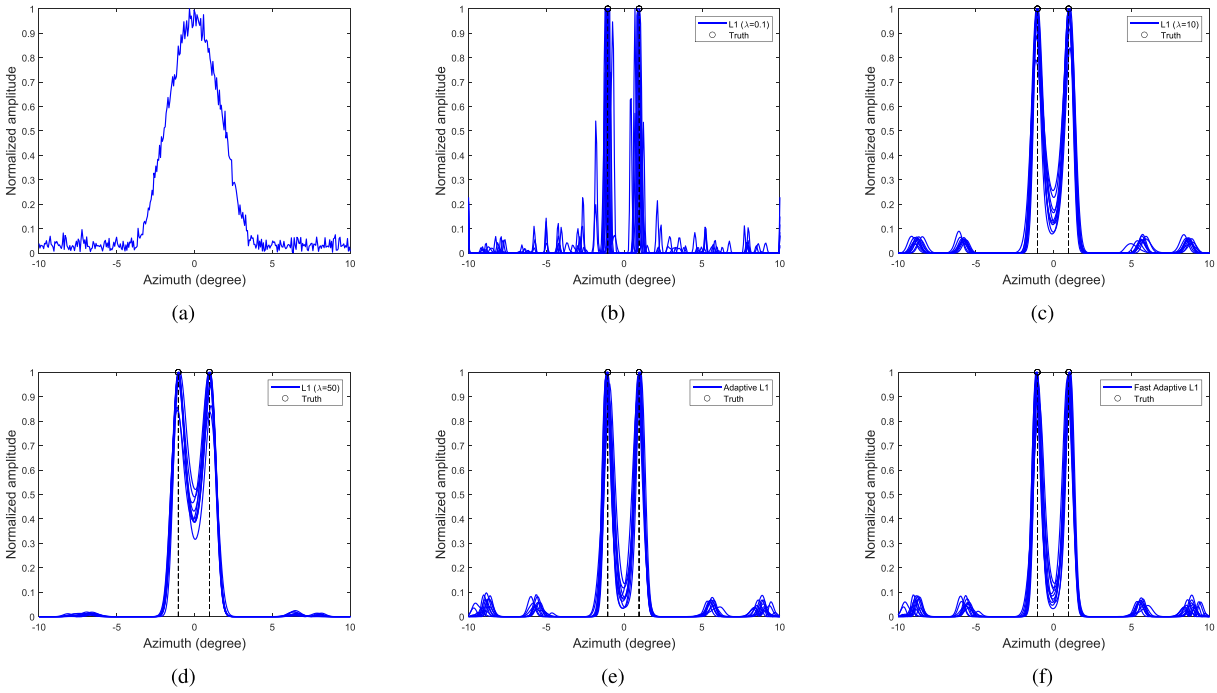

Fig. 4. Point target profile result. (a) Real beam echo. (b) Simulation result of traditional L_1-IRN method when $\lambda = 0.1$. (c) Result of traditional L_1-IRN method when $\lambda = 10$. (d) Result of traditional L_1-IRN method when $\lambda = 50$. (e) Result of adaptive L_1-IRN method. (f) Result of the fast adaptive L_1-IRN method.

TABLE III
MSE VALUES OF THE THREE METHODS UNDER 20 DB SNR

Method	MSE
Traditional L_1-IRN method ($\lambda = 0.1$)	0.78×10^{-5}
Traditional L_1-IRN method ($\lambda = 10$)	7.57×10^{-5}
Traditional L_1-IRN method ($\lambda = 50$)	12.1×10^{-5}
Adaptive L_1-IRN method	5.50×10^{-5}
Fast adaptive L_1-IRN method	5.71×10^{-5}

where m is the true value, $\hat{m}_i$ is the estimated value of $\mathbf{m}$ at ith direction, and S is the total number of Monte Carlo trials, respectively. The MSE values of the three methods under 20 dB SNR are shown in Table III. It is observable that the smallest MSE value is achieved by the traditional L_1-IRN method when $\lambda = 0.1$. However, under this condition, false targets will appear. The false alarm phenomenon is unacceptable for radar applications, which is not conducive to subsequent target detection and recognition. Whereas, the proposed method exhibits a lower MSE than the traditional L_1-IRN method under $\lambda = 10$ and 50, and comparably aligns with the adaptive L_1-IRN method. This indicates that the acceleration process of the proposed method has little impact on the reconstruction quality.

The performance of the super-resolution method is further demonstrated by introducing the peak-to-valley ratio (PVR), which is mainly used to describe the proportional relationship between the maximum amplitude (peak) and the minimum amplitude (valley value) of the signal, as depicted by Fig. 5. The higher the PVR value, the better the ability to distinguish

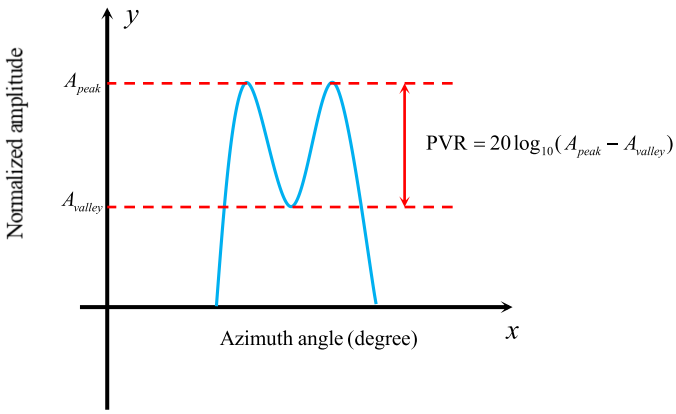

Fig. 5. Peak-to-valley ratio.

between two adjacent objects. Peak-to-valley ratio can be defined as follows:

$$\mathrm{PVR} = 20\log_{10}(A_{\mathrm{peak}} - A_{\mathrm{valley}}) \tag{45}$$

where A_{peak} and A_{valley} indicate the maximum and minimum amplitude of the signal, repectively. The PVR values of the three methods under 20 dB SNR are shown in Table IV.

Mirroring the circumstances of MSE, observations indicate that the traditional L_1 method generates a substantial number of falsified targets in the imaging results when $\lambda = 0.1$. Consequently, the miscalculations of peak and valley values hinder the accurate computation of PVR. The PVR value of the adaptive L_1-IRN method and fast adaptive L_1-IRN method is larger than

TABLE IV
PVR VALUES OF THE THREE METHODS UNDER 20 DB SNR

Method	PVR
Traditional L_1-IRN method ($\lambda = 0.1$)	–
Traditional L_1-IRN method ($\lambda = 10$)	-1.77
Traditional L_1-IRN method ($\lambda = 50$)	-5.26
Adaptive L_1-IRN method	-0.87
Fast adaptive L_1-IRN method	-0.82

TABLE V
RUNNING TIMES OF THE THREE METHODS

Method	Running time
Traditional L_1-IRN method ($\lambda = 0.1$)	0.22 s
Traditional L_1-IRN method ($\lambda = 10$)	0.26 s
Traditional L_1-IRN method ($\lambda = 50$)	0.27 s
Adaptive L_1-IRN method	0.23 s
Fast adaptive L_1-IRN method	0.16 s

TABLE VI
SIMULATION PARAMETERS OF THE SURFACE TARGET

Parameter	Value
Carrier frequency	30 GHz
Scanning speed	60°/s
Main lobe width	3°
Signal bandwidth	5 MHz
Pulse time width	2 μs
Pulse repetition frequency	1000 Hz
Platform velocity	30 m/s
Slant range	3000 m

the traditional L_1-IRN method under $\lambda = 10$ and 50, which proves that its ability to distinguish targets is stronger than traditional L_1-IRN method. The PVR value of the fast adaptive L_1-IRN method is almost the same as the adaptive L_1-IRN method, which indicates that the acceleration process has no effect on the ability to distinguish between targets. The running times of the three methods are shown in Table V.

It is apparent that the fast adaptive L_1-IRN method exhibits the shortest running time. In summary, this method reduces the algorithm's computational complexity while maintaining the resolution and parameter-free capabilities. The simulation results demonstrate the feasibility of employing the fast adaptive L_1-IRN method for point target scenarios.

B. Surface Target Simulation

To further validate the effectiveness of the fast adaptive L_1-IRN method, we conducted surface target simulation in this section. The parameters of the simulation environment are presented in Table VI.

1) Surface Target Results: The original scene of the surface target is shown in Fig. 6. The echo with a SNR of 20 dB is shown

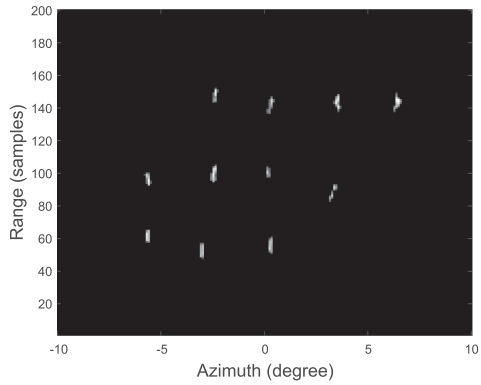

Fig. 6. Original scene of the surface target.

TABLE VII
MSE VALUES OF THE THREE METHODS UNDER 20 DB SNR

Method	MSE
Traditional L_1-IRN method ($\lambda = 0.5$)	5.59×10^{-4}
Traditional L_1-IRN method ($\lambda = 20$)	4.50×10^{-4}
Traditional L_1-IRN method ($\lambda = 400$)	4.89×10^{-4}
Adaptive L_1-IRN method	4.12×10^{-4}
Fast adaptive L_1-IRN method	4.16×10^{-4}

in Fig. 7(a). We have conducted multiple sets of Monte Carlo experiments, and the results of one set of experiments are shown in Fig. 7(b)–(f). The simulation result of the traditional L_1-IRN method when $\lambda = 0.5$ is shown in Fig 7(b). The simulation result of the traditional L_1-IRN method when $\lambda = 20$ is shown in Fig. 7(c). The imaging result is noticeably superior to those obtained when $\lambda = 0.5$, with false targets eliminated despite a slight decrease in resolution. The simulation result of the traditional L_1-IRN method when $\lambda = 400$ is shown in Fig. 7(d). It can be observed that with the increase in the regularization parameter λ, the azimuthal resolution of the imaging gradually decreases. Therefore, the traditional L_1IRN method requires adjusting an optimal λ to achieve the best imaging result, which does not facilitate the practical applications.

On the contrary, the simulation result of the adaptive L_1-IRN method is illustrated in Fig. 7(e). It can be seen that the resolution and noise suppression effect of this method are better than the traditional method with different λ. However, this method suffers a high computational complexity, resulting in a running time of 76.86 s. Leveraging the dimension reduction strategy, the proposed fast adaptive L_1-IRN method achieves almost the same imaging result, which is displayed in Fig. 7(f) with a running time of 32.81 s. The proposed fast adaptive L_1-IRN method achieves algorithm acceleration with minimal compromise on imaging quality.

2) Quantitative Analysis: In this section, the MSE values of three methods at a 20 dB SNR are provided, as shown in Table VII.

The structural similarity index (SSIM) is introduced to analyze the performance of image reconstruction. SSIM is an index

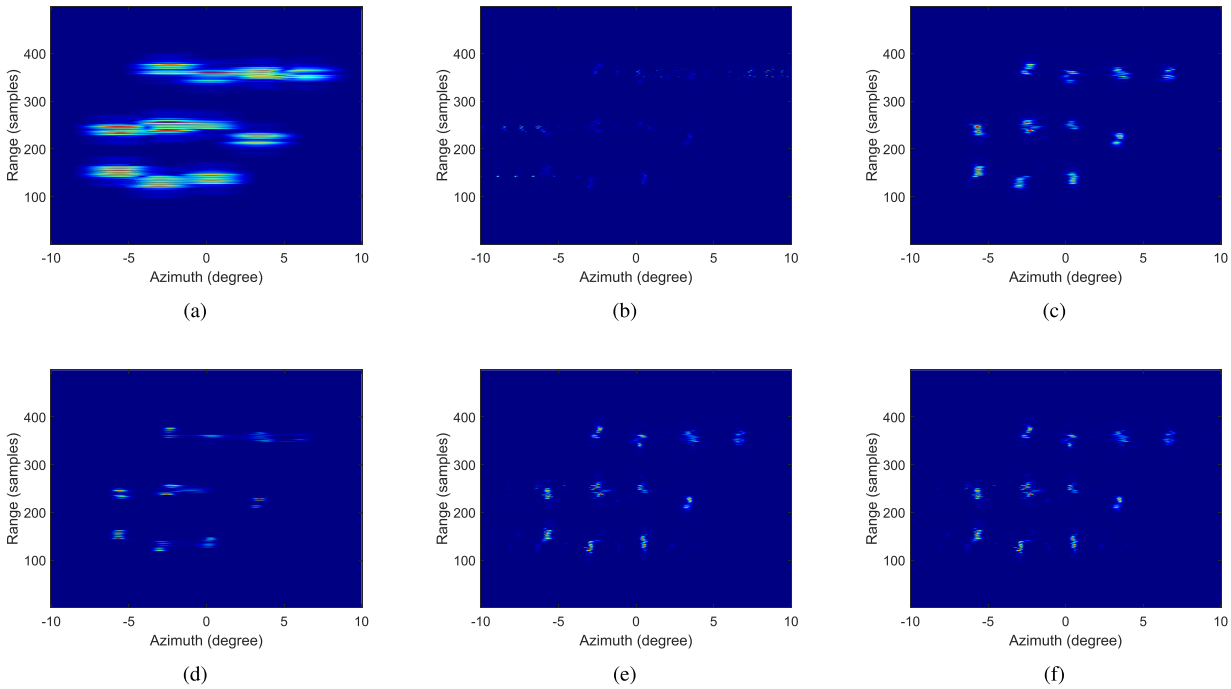

Fig. 7. Surface target profile result. (a) Real beam echo. (b) Simulation result of traditional L_1-IRN method when $\lambda = 0.5$. (c) Result of traditional L_1-IRN method when $\lambda = 20$. (d) Result of traditional L_1-IRN method when $\lambda = 400$. (e) Result of adaptive L_1-IRN method. (f) Result of the fast adaptive L_1-IRN method.

TABLE VIII
SSIM VALUES OF THE THREE METHODS UNDER 20 DB SNR

Method	SSIM
Traditional L_1-IRN method ($\lambda = 0.5$)	0.64
Traditional L_1-IRN method ($\lambda = 20$)	0.68
Traditional L_1-IRN method ($\lambda = 400$)	0.64
Adaptive L_1-IRN method	0.69
Fast adaptive L_1-IRN method	0.69

TABLE IX
RUNNING TIME OF THE THREE METHODS

Method	Running time
Traditional L_1-IRN method ($\lambda = 0.5$)	74.68 s
Traditional L_1-IRN method ($\lambda = 20$)	79.62 s
Traditional L_1-IRN method ($\lambda = 400$)	83.66 s
Adaptive L_1-IRN method	76.86 s
Fast adaptive L_1-IRN method	32.81 s

to measure the visual similarity of two images, which is affected by the brightness, contrast, and structure of the images. SSIM can be defined as follows:

$$\mathrm{SSIM}(\mathbf{M}, \mathbf{Y}) = \frac{(2\mu_{\mathbf{M}}\mu_{\mathbf{Y}} + c_1)(2\sigma_{\mathbf{MY}} + c_2)}{(\mu_{\mathbf{M}}^2 + \mu_{\mathbf{Y}}^2 + c_1)(\sigma_{\mathbf{M}}^2 + \sigma_{\mathbf{Y}}^2 + c_2)} \quad (46)$$

where $\mathbf{M}$ is the matrix of the results of each super-resolution method, which can be specified as $\mathbf{M} = [\mathbf{m}_1, \mathbf{m}_2, \ldots, \mathbf{m}_L]$. $\mathbf{Y}$ is the echo matrix, which can be specified as $\mathbf{Y} = [\mathbf{y}_1, \mathbf{y}_2, \ldots, \mathbf{y}_L]$. $\mu_{\mathbf{M}}$ is the average value of $\mathbf{M}$, $\mu_{\mathbf{Y}}$ is the mean value of $\mathbf{Y}$, $\sigma_{\mathbf{M}}$ is the variance of $\mathbf{M}$, $\sigma_{\mathbf{Y}}$ is the variance of $\mathbf{Y}$, and $\sigma_{\mathbf{MY}}$ is the covariance of $\mathbf{M}$ and $\mathbf{Y}$, respectively. c_1 and c_2 are constant. The SSIM values of the simulation results of the three super-resolution methods are shown in Table VIII.

Through comparison, the SSIM and MSE values of traditional L_1-IRN method at $\lambda = 0.5$ and 400 are inferior, leading to unsatisfactory imaging results. Conversely, the SSIM and MSE value of the traditional L_1-IRN method at $\lambda = 20$ exhibit relative improvement, likely because $\lambda = 20$ is closer to the optimal parameter. Notably, the adaptive L_1-IRN method outperforms other techniques in terms of both SSIM and MSE values, indicating a simulation outcome more similar to the original scene. Moreover, the SSIM and MSE values of the fast adaptive L_1-IRN method nearly match those of the adaptive L_1-IRN method, suggesting that the acceleration process does not compromise imaging quality. Table IX presents the runtime performance of these three methods.

It can be seen that the fast adaptive L_1-IRN method has the shortest running time. In summary, the fast adaptive L_1-IRN method can greatly reduce the computational complexity of the algorithm while maintaining adaptability and high azimuth resolution. The simulation results show that the fast adaptive L_1-IRN method is feasible to the surface target.

V. MEASURED DATA RESULTS

In the previous section, the feasibility of the proposed method was demonstrated through point and surface target simulation

Fig. 8. Optical scene.

TABLE X
EXPERIMENTAL PARAMETERS

Parameter	Value
Carrier frequency	9.4 GHz
Scanning speed	$72^\circ/\mathrm{s}$
Scanning range	-45°–45°
Bandwidth	75 MHz
PRF	204 Hz
Main lobe width	5.1°

experiments. To further validate the imaging performance of the proposed method, two sets of experimental measured data are utilized.

A. Analysis of Experimental Measured Data 1

1) Imaging Results: The real scene depicted in Fig. 8 reveals several groups of ships, with notably short azimuthal distances between two boats highlighted in the red box. Experimental parameters are detailed in Table X. As illustrated in Fig. 9(a), the echo image fails to distinguish between the two ships directly. The super-resolution imaging results, presented in Fig. 9(b)–(f), exhibit varying outcomes based on different values of λ.

When $\lambda = 0.01$, the imaging result of the traditional L_1-IRN method is shown in Fig. 9(b), which contains abundant false targets. When $\lambda = 0.1$, the imaging result of the traditional L_1-IRN method is shown in Fig. 9(c). It can be seen that the number of false targets has decreased, but the ships are not clear. When $\lambda = 10$, the imaging result of the traditional L_1-IRN method is shown in Fig. 9(d), where it can be seen that the ships are more visible, but they are not completely separated. Through traditional L_1-IRN simulation under different parameters λ, it is observed that continuous adjustment of λ is necessary to achieve the best imaging result. The imaging result obtained using the adaptive L_1-IRN method is depicted in Fig. 9(e), showing its ability to distinguish between the two ships. Notably, the resulting image is clearer and exhibits higher azimuth resolution. The imaging result of the fast adaptive L_1-IRN method is shown in Fig. 9(f). Comparing Fig. 9(e) and (f), it can be seen that a small number of weak targets in Fig. 9(f) are disappeared. This phenomenon occurs due to the dimensionality reduction of the echo matrix, which essentially reduces the observation information used for super-resolution processing. Moderate dimensionality reduction only slightly affects imaging quality, and a good reconstruction can still be achieved for the main target of interest, as shown in the red box of the ships in Fig. 9(f). Conversely, excessive dimensionality reduction significantly degrades imaging quality, despite providing lower computational complexity, which is the tradeoff for the "fast" of the proposed method.

TABLE XI
IMAGE ENTROPY OF THE THREE METHODS

Method	Image entropy
Traditional L_1-IRN method ($\lambda = 0.01$)	2.06
Traditional L_1-IRN method ($\lambda = 0.1$)	2.44
Traditional L_1-IRN method ($\lambda = 10$)	4.34
Adaptive L_1-IRN method	2.11
Fast adaptive L_1-IRN method	2.09

2) Quantitative Analysis: Image entropy is introduced to quantify the quality of the imaging results of each method. The higher image entropy means that the distribution of pixel values is more uniform and the information or complexity of the image is higher. On the contrary, lower image entropy means that the distribution of pixel values is more concentrated and the information is lower. Image entropy can be defined as follows:

$$H(X) = -\sum_{i=1}^{n} p_i \log_2 p_i \tag{47}$$

where p_i represents the probability of gray level i appearing in the image. The image entropy of the three methods is shown in Table XI.

From Table XI, although the traditional L_1-IRN method exhibits lower image entropy at $\lambda = 0.01$, the imaging results in Fig. 9(b) indicate that this parameter introduces more false targets, resulting in the split scatters for the two ships. This is actually detrimental to radar imaging. It can be seen that the image entropy of the adaptive L_1-IRN method is lower than the traditional L_1-IRN method under $\lambda = 0.1$ and 10, which indicates that the image information distribution of the imaging result of this method is more concentrated and the imaging result is better. The image entropy of the fast adaptive L_1-IRN method is approximately the same as the adaptive L_1-IRN method, which indicates that the acceleration process has little effect on the resolution. The running time of the three methods is shown in Table XII.

It can be seen that the fast adaptive L_1-IRN method has the least running time. In conclusion, the fast adaptive L_1-IRN method can greatly reduce the computational complexity of the algorithm while maintaining the resolution and noise suppression effect of the adaptive L_1-IRN method. The experimental results show that the fast adaptive L_1-IRN method can be applied in practice.

3) Profile Analysis: Range bin of 1000 m of the profile results of the three methods are extracted from Fig. 9, as depicted in

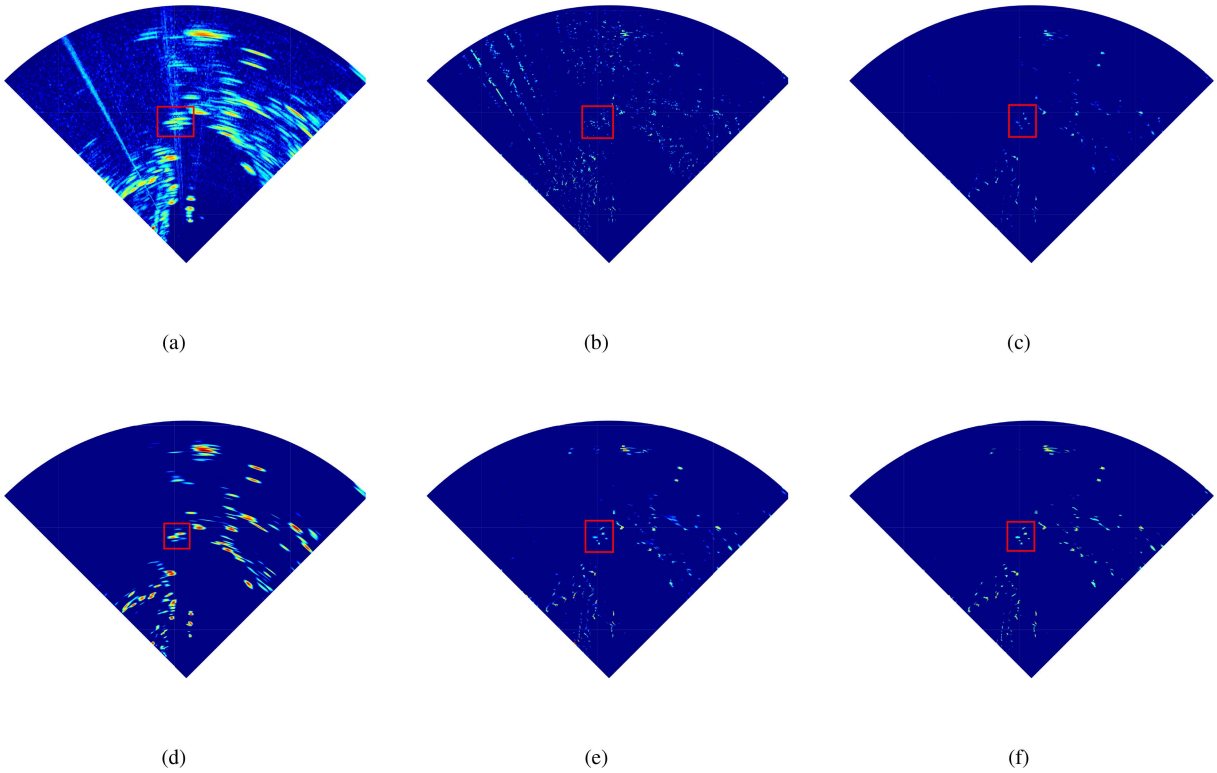

Fig. 9. Measured data results. (a) Real beam echo. (b) Imaging results of traditional L_1-IRN method with $\lambda = 0.01$. (c) Imaging results of traditional L_1-IRN method with $\lambda = 0.1$. (d) Imaging results of traditional L_1-IRN method with $\lambda = 10$. (e) Imaging results of adaptive L_1-IRN method. (f) Imaging results of fast adaptive L_1-IRN method.

TABLE XII
RUNNING TIME OF THE THREE METHODS

Method	Running time
Traditional L_1-IRN method ($\lambda = 0.01$)	217.52 s
Traditional L_1-IRN method ($\lambda = 0.1$)	219.03 s
Traditional L_1-IRN method ($\lambda = 10$)	224.47 s
Adaptive L_1-IRN method	215.18 s
Fast adaptive L_1-IRN method	76.06 s

TABLE XIII
3 DB BANDWIDTHS FOR THE THREE METHODS

Method	3dB azimuthal width (°)
Traditional L_1-IRN method ($\lambda = 0.01$)	0.22
Traditional L_1-IRN method ($\lambda = 0.1$)	0.76
Traditional L_1-IRN method ($\lambda = 10$)	2.83
Adaptive L_1-IRN method	0.70
Fast adaptive L_1-IRN method	0.72

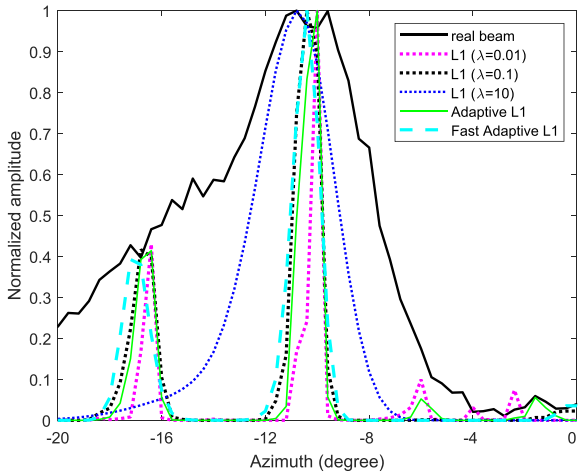

Fig. 10. Profile results of the echo and imaging results from 1000 m range bin in Fig. 9.

Fig. 10. The 3 dB bandwidths of real beam echo and these methods are illustrated in Table XIII.

Observations indicate that the traditional L_1-IRN method achieves the smallest 3 dB azimuthal width when $\lambda = 0.01$, but there will be numerous false targets. When $\lambda = 10$, traditional L_1-IRN method has improved the issue of erroneous targets appearing. However, the 3 dB azimuthal width is wide. When $\lambda = 0.1$, traditional L_1-IRN method has found a balance between the appearance of erroneous targets and reducing the 3 dB azimuthal width, but it requires manual adjustment of user parameters and has high computational complexity. Whereas,

Fig. 11. Optical scene.

the proposed method exhibits a lower 3 dB azimuthal width than the traditional L_1-IRN method under $\lambda = 10$, and comparably aligns with the adaptive L_1-IRN method. This indicates that the acceleration process of the proposed method has nearly no impact on the super-resolution quality.

B. Analysis of Experimental Measured Data 2

1) Imaging Results: The second set of the measured data was recorded at the University of Electronic Science and Technology (UESTC), Ginkgo Road, Chengdu, China, and Fig. 11 shows the optical image (from Google Earth). The real scene reveals several groups of ginkgo trees arranged vertically on both sides of the road. Experimental parameters are the same as in Table X. As illustrated in Fig. 12(a), the azimuth resolution of echo image is poor, and neighboring trees further back in the image are indistinguishable.

The super-resolution imaging results, presented in Fig. 12(b)–(f), exhibit varying outcomes based on different values of λ. When $\lambda = 1000$, the imaging result of the traditional L_1-IRN method is shown in Fig. 12(b), which contains abundant false targets. When $\lambda = 10000$, the imaging result of the traditional L_1-IRN method is shown in Fig. 12(c). It can be seen that the number of false targets has decreased, but the trees are not clear. When $\lambda = 400000$, the imaging result of the traditional L_1-IRN method is shown in Fig. 12(d), where it can be seen that the trees are more visible. However, many weak targets disappear. The adaptive L_1-IRN method's output, illustrated in Fig. 12(e), effectively discriminates between trees, offering a clearer image and enhancing azimuth resolution. The fast adaptive L_1-IRN method, visualized in Fig. 12(f), maintains similar imaging quality to the former method but with reduced computational demands.

2) Quantitative Analysis: The image entropy of the three methods is shown in Table XIV.

From Table XIV, although the traditional L_1-IRN method exhibits lower image entropy at $\lambda = 400000$, the imaging results in Fig. 12(d) indicate that this parameter makes a large number of targets disappear, which is actually detrimental to radar imaging. It can be seen that the image entropy of the adaptive L_1-IRN method is lower than the traditional L_1-IRN method under $\lambda = 1000$ and 10000, which indicates that the image information distribution of the imaging result of this method is more concentrated and the imaging result is better. The image entropy of the fast adaptive L_1-IRN method is approximately the same as the adaptive L_1-IRN method, which indicates that the acceleration process has little effect on the resolution. The running time of the three methods is shown in Table XV. The fast adaptive L_1-IRN method demonstrates the shortest runtime among the compared techniques.

In summary, the proposed approach dramatically lowers computational complexity while preserving resolution and noise suppression capabilities akin to the adaptive L_1-IRN method. The experimental results support the practical applicability of the fast adaptive L_1-IRN method.

TABLE XIV
IMAGE ENTROPY OF THE THREE METHODS

Method	Image entropy
Traditional L_1-IRN method ($\lambda = 1000$)	0.27
Traditional L_1-IRN method ($\lambda = 10000$)	0.26
Traditional L_1-IRN method ($\lambda = 400000$)	0.09
Adaptive L_1-IRN method	0.23
Fast adaptive L_1-IRN method	0.21

TABLE XV
RUNNING TIME OF THE THREE METHODS

Method	Running time
Traditional L_1-IRN method ($\lambda = 1000$)	172.41 s
Traditional L_1-IRN method ($\lambda = 10000$)	191.92 s
Traditional L_1-IRN method ($\lambda = 400000$)	536.47 s
Adaptive L_1-IRN method	101.87 s
Fast adaptive L_1-IRN method	67.44 s

TABLE XVI
COMPLEXITY COMPARISON BETWEEN ADAPTIVE L_1-IRN METHOD AND FAST ADAPTIVE L_1-IRN METHOD

Scanning scope (°)	N	t_a	t_{fa}	t_a/t_{fa}
−4.5°−4.5°	150	8.00 s	7.79 s	1.03
−9°−9°	300	29.21 s	27.26 s	1.07
−18°−18°	600	122.83 s	109.68 s	1.12
−27°−27°	900	303.49 s	222.75 s	1.36
−36°−36°	1200	614.82 s	252.34 s	2.43

C. Comparison of Complexity Between Adaptive L_1-IRN Method and Fast Adaptive L_1-IRN Method

The computational complexity of adaptive L_1-IRN method and fast adaptive L_1-IRN method with varying scanning scope from $-4.5\,^\circ - 4.5\,^\circ$ to $-36\,^\circ - 36\,^\circ$ is investigated. Correspondingly, N varies from 150 to 1200 (PRF = 1000 Hz and $\omega =$

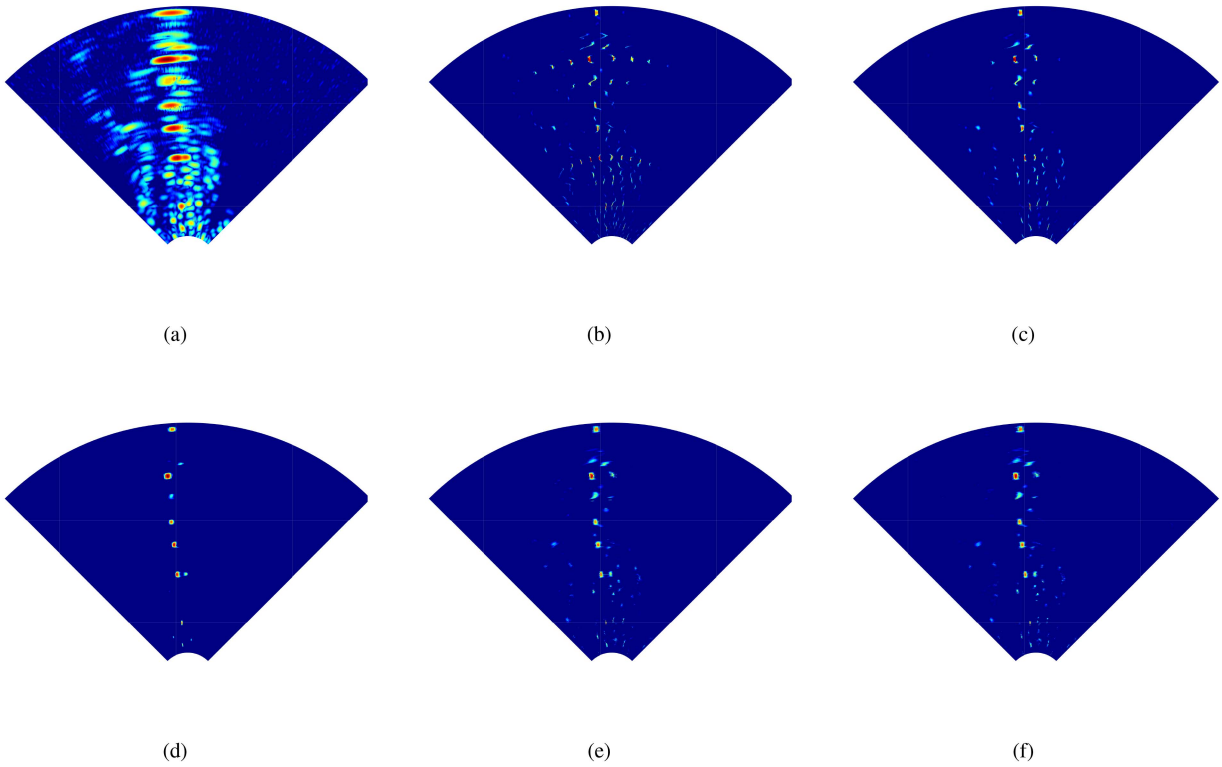

Fig. 12. Measured data results. (a) Real beam echo, (b) Imaging results of traditional L_1-IRN method with $\lambda = 1000$. (c) Imaging results of traditional L_1-IRN method with $\lambda = 10\,000$. (d) Imaging results of traditional L_1-IRN method with $\lambda = 400\,000$. (e) Imaging results of adaptive L_1-IRN method. (f) Imaging results of fast adaptive L_1-IRN method.

$60^\circ/\text{s}$). The running time of adaptive L_1-IRN method and fast adaptive L_1-IRN method, referred to as t_a and t_{fa}, respectively, are recorded in seconds in Table XVI. We can observe that as N increases, the computational savings provided by fast adaptive L_1-IRN method become more significant compared with adaptive L_1-IRN method.

VI. Conclusion

In this article, we propose a novel fast adaptive L_1 iterative reweighted imaging method for forward-looking radar super-resolution. The proposed method adapts effectively to different environments while maintaining robustness. Unlike traditional L_1-IRN super-resolution techniques, our approach eliminates the need for manual parameter tuning. Furthermore, compared to conventional adaptive L_1-IRN, our method significantly reduces computational complexity from $O(JN^3)$ to $O(JN^2a)$, making it especially suitable for wide-area radar super-resolution imaging tasks.

References

[1] M. Mousavi, A. Colliander, J. Z. Miller, and J. S. Kimball, "A novel approach to map the intensity of surface melting on the antarctica ice sheet using SMAP l-band microwave radiometry," *IEEE J. Sel. Topics Appl. Earth Observ. Remote Sens.*, vol. 15, pp. 1724–1743, 2022.

[2] S. Young, S. Harrah, and M. d. Haag, "Real-time integrity monitoring of stored geo-spatial data using forward-looking remote sensing technology [aircraft navigation/displays]," in *Proc. 21st Digit. Avionics Syst. Conf.*, 2002, pp. 11D1–11D1.

[3] R. Zhu, G. Lu, L. Liang, and Z. Zhang, "Forward-looking imaging method of airborne array radar based on uniform circular array," in *Proc. IEEE 22nd Int. Conf. Commun. Technol. (ICCT)*, 2022, pp. 1852–1858.

[4] M. Ressler, L. Nguyen, F. Koenig, D. Wong, and G. Smith, "The army research laboratory (ARL) synchronous impulse reconstruction (sire) forward-looking radar," in *Unmanned Systems Technology IX*, vol. 6561. Bellingham, WA, USA: SPIE, 2007, pp. 35–46.

[5] A. Gambardella and M. Migliaccio, "On the superresolution of microwave scanning radiometer measurements," *IEEE Geosci. Remote Sens. Lett.*, vol. 5, no. 4, pp. 796–800, Oct. 2008.

[6] L. H. Nguyen, T. T. Ton, D. C. Wong, and M. A. Ressler, "Signal processing techniques for forward imaging using ultrawideband synthetic aperture radar," in *Unmanned Ground Vehicle Technology V*, vol. 5083. Bellingham, WA, USA: SPIE, 2003, pp. 505–518.

[7] L. H. Nguyen and C. Le, "3D imaging for millimeter-wave forward-looking synthetic aperture radar (SAR)," in *Passive and Active Millimeter-Wave Imaging XXIII*, vol. 11411. Bellingham, WA, USA: SPIE, 2020, pp. 83–94.

[8] D. Mao, Y. Zhang, Y. Zhang, Y. Huang, and J. Yang, "Super-resolution doppler beam sharpening method using fast iterative adaptive approach-based spectral estimation," *J. Appl. Remote Sens.*, vol. 12, no. 1, 2018, Art. no. 015020.

[9] Y. Zhang, D. Mao, Q. Zhang, Y. Zhang, Y. Huang, and J. Yang, "Airborne forward-looking radar super-resolution imaging using iterative adaptive approach," *IEEE J. Sel. Topics Appl. Earth Observ. Remote Sens.*, vol. 12, no. 7, pp. 2044–2054, Jul. 2019.

[10] Y. Zhang, Y. Zhang, Y. Huang, W. Li, and J. Yang, "Angular superresolution for scanning radar with improved regularized iterative adaptive approach," *IEEE Geosci. Remote Sens. Lett.*, vol. 13, no. 6, pp. 846–850, Jun. 2016.

[11] J. Luo et al., "Two-dimensional angular super-resolution for airborne real aperture radar by fast conjugate gradient iterative adaptive approach," *IEEE Trans. Aerosp. Electron. Syst.*, vol. 59, no. 6, pp. 9480–9500, Dec. 2023.

[12] H. Dropkin and C. Ly, "Superresolution for scanning antenna," in *Proc. 1997 IEEE Nat. Radar Conf.*, IEEE, 1997, pp. 306–308.

[13] J. Lu, L. Zhang, Y. Quan, Z. Meng, and Y. Cao, "Parametric azimuth-variant motion compensation for forward-looking multichannel SAR imagery," *IEEE Trans. Geosci. Remote Sens.*, vol. 59, no. 10, pp. 8521–8537, Oct. 2021.
[14] H. Chen et al., "Bayesian forward-looking superresolution imaging using Doppler deconvolution in expanded beam space for high-speed platform," *IEEE Trans. Geosci. Remote Sens.*, vol. 60, 2021, Art. no. 5105113.
[15] K. Tan, X. Lu, J. Yang, W. Su, and H. Gu, "A novel Bayesian super-resolution method for radar forward-looking imaging based on Markov random field model," *Remote Sens.*, vol. 13, no. 20, 2021, Art. no. 4115.
[16] W. Li, M. Li, L. Zuo, H. Sun, H. Chen, and Y. Li, "Forward-looking super-resolution imaging for sea-surface target with multi-prior Bayesian method," *Remote Sens.*, vol. 14, no. 1, 2021, Art. no. 26.
[17] Y. Zhang, X. Tuo, Y. Huang, and J. Yang, "A TV forward-looking super-resolution imaging method based on TSVD strategy for scanning radar," *IEEE Trans. Geosci. Remote Sens.*, vol. 58, no. 7, pp. 4517–4528, Jul. 2020.
[18] Z. Shu, Z. Zong, L. Huang, and L. Huang, "Forward-looking radar super-resolution imaging combined TSVD with L1 norm constraint," in *Proc. 2019 IEEE Int. Geosci. Remote Sens. Symp.*, IEEE, 2019, pp. 2559–2562.
[19] X. Tuo, Y. Zhang, Y. Huang, and J. Yang, "Fast sparse-TSVD super-resolution method of real aperture radar forward-looking imaging," *IEEE Trans. Geosci. Remote Sens.*, vol. 59, no. 8, pp. 6609–6620, Aug. 2021.
[20] Y. Zhang, Q. Zhang, Y. Zhang, Y. Huang, and J. Yang, "Superresolution of radar forward-looking imaging based on accelerated tv-sparse method," *IEEE J. Sel. Topics Appl. Earth Observ. Remote Sens.*, vol. 14, pp. 92–102, 2020.
[21] X. Tuo, Y. Zhang, Y. Huang, and J. Yang, "A fast sparse azimuth super-resolution imaging method of real aperture radar based on iterative reweighted least squares with linear sketching," *IEEE J. Sel. Topics Appl. Earth Observ. Remote Sens.*, vol. 14, pp. 2928–2941, 2021.
[22] J. H. Ender, "On compressive sensing applied to radar," *Signal Process.*, vol. 90, no. 5, pp. 1402–1414, 2010.
[23] Y.-S. Yoon and M. G. Amin, "Compressed sensing technique for high-resolution radar imaging," in *Signal Processing, Sensor Fusion, and Target Recognition XVII*, vol. 6968. Bellingham, WA, USA: SPIE, 2008, pp. 506–515.
[24] M. Feng, X. Tuo, Y. Zhang, D. Mao, Y. Huang, and J. Yang, "Regularization method with weak-depended on parameter for forward-looking super-resolution imaging," in *Proc. 2023 IEEE Int. Geosci. Remote Sens. Symp.*, IEEE, 2023, pp. 8102–8105.
[25] H. Chen et al., "Cross-range resolution enhancement for DBS imaging in a scan mode using aperture-extrapolated sparse representation," *IEEE Geosci. Remote Sens. Lett.*, vol. 14, no. 9, pp. 1459–1463, Sep. 2017.
[26] Y. Zhang et al., "Fast inverse-scattering reconstruction for airborne high-squint radar imagery based on doppler centroid compensation," *IEEE Trans. Geosci. Remote Sens.*, vol. 60, 2021, Art. no. 5205517.
[27] Y. Zhang et al., "Resolution enhancement for large-scale real beam mapping based on adaptive low-rank approximation," *IEEE Trans. Geosci. Remote Sens.*, vol. 60, 2022, Art. no. 5116921.
[28] Y. Zhang, W. Li, Y. Zhang, Y. Huang, and J. Yang, "A fast iterative adaptive approach for scanning radar angular superresolution," *IEEE J. Sel. Topics Appl. Earth Observ. Remote Sens.*, vol. 8, no. 11, pp. 5336–5345, Nov. 2015.
[29] X. Tuo et al., "Two-step dimension reduction strategy for real-aperture radar fast super-resolution imaging," *IEEE Geosci. Remote Sens. Lett.*, vol. 19, 2022, Art. no. 4025505.

Jiawei Luo (Student Member, IEEE) received the B.S. degree in engineering from the School of Electronic and Information Engineering, Changchun University of Science and Technology, Changchun, China, in 2019. He is currently working toward the Ph.D. degree with the School of Information and Communication Engineering, University of Electronic Science and Technology of China (UESTC), Chengdu, China.

His research interests include radar signal processing and inverse problem in radar imaging.

Yulin Huang (Senior Member, IEEE) received the B.S. and Ph.D. degrees in electronic engineering from the University of Electronic Science and Technology of China (UESTC), Chengdu, China, in 2002, and 2008, respectively.

From 2013 to 2014, he was a Visiting Researcher with the University of Houston, Houston, TX, USA. Since 2016, he has been a Professor with the School of Information and Communication Engineering, UESTC. He has authored more than 80 journal and conference papers. His research interests include synthetic aperture radar, target detection and recognition, artificial intelligence, and machine learning.

Dr. Huang is a Member of the IEEE Aerospace and Electronic Systems Society.

Ruitao Li received the B.S. degree in electronic information from the School of Information Science and Engineering, Lanzhou University, Lanzhou, China, in 2018. He is currently working toward the M.S. degree in information and communication engineering with the University of Electronic Science and Technology of China (UESTC), Chengdu, China.

His research interests include radar imaging and sparse reconstruction.

Deqing Mao (Member, IEEE) received the B.S. degree from the School of Electronic Engineering, Chengdu University of Information Technology, Chengdu, China, and the Ph.D. degree from the School of Information and Communication Engineering, University of Electronic Science and Technology of China (UESTC), Chengdu, both in signal and information processing, in 2014 and 2022.

From 2020 to 2021, he has been a Visiting Ph.D. Student with the Technology University of Delft, Delft, The Netherlands. His research interests include radar signal processing and inverse problem in radar imaging.

Yongchao Zhang (Member, IEEE) received the B.S. degree in electronic information engineering from Hainan University, Haikou, China, in 2011, and the Ph.D. degree in signal and information processing from the School of Information and Communication Engineering, University of Electronic Science and Technology of China (UESTC), Chengdu, China, in 2018.

From 2016 to 2017, he was a Visiting Student with Lund University, Lund, Sweden. He is currently an Associate Research Fellow with the School of Information and Communication Engineering, UESTC. His research interests include array signal processing and inverse problems in radar applications.

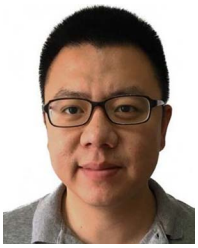

Yin Zhang (Member, IEEE) received the B.S. and Ph.D. degrees in electronic information engineering from the University of Electronic Science and Technology of China (UESTC), Chengdu, China, in 2008 and 2016, respectively.

From 2015 to 2016, he was a Visiting Student with the University of Delaware, Newark, DE, USA. He is currently an Associate Research Fellow with the School of Information and Communication Engineering, UESTC. His research interests include radar imaging and signal processing in related radar applications.

Jianyu Yang (Member, IEEE) received the B.S. degree in radar technology from the National University of Defense Technology, Changsha, China, in 1984, and the M.S. and Ph.D. degrees in signal and information processing from the University of Electronic Science and Technology of China (UESTC), Chengdu, China, in 1987 and 1991, respectively.

Since 1999, he has been a Professor with the School of Information and Communication Engineering, UESTC. In 2005, he visited Massachusetts Institute of Technology, USA. He has authored more than 120 journal and conference papers. His research interests include synthetic aperture radar and statistical signal processing.

Dr. Yang is a Fellow of the Chinese Institute of Electronics.